Control of Interface Order by Inverse Quasi-Epitaxial Growth of Squaraine/Fullerene Thin Film Photovoltaics

Jeramy D. Zimmerman,[†] Brian E. Lassiter,[‡] Xin Xiao,[†] Kai Sun,[‡] Andrei Dolocan,[§] Raluca Gearba,[⊥] David A. Vanden Bout,[⊥] Keith J. Stevenson,[⊥] Piyumie Wickramasinghe,[∥] Mark E. Thompson,[∥] and Stephen R. Forrest[†,‡,#,*]

[†]Department of Electrical Engineering and Computer Science, University of Michigan, Ann Arbor, Michigan 48109, United States, [‡]Materials Science and Engineering, University of Michigan, Ann Arbor, Michigan 48109, United States, [§]Texas Materials Institute, The University of Texas at Austin, Austin, Texas 78712, United States, [⊥]Energy Frontier Research Center (EFRC:CST), The University of Texas at Austin, Austin, Texas 78712, United States, [∥]Department of Chemistry, University of Southern California, Los Angeles, California 90089, United States, and [#]Department of Physics, University of Michigan, Ann Arbor, Michigan 48109, United States

ABSTRACT It has been proposed that interface morphology affects the recombination rate for electrons and holes at donor–acceptor heterojunctions in thin film organic photovoltaic cells. The optimal morphology is one where there is disorder at the heterointerface and order in the bulk of the thin films, maximizing both the short circuit current and open circuit voltage. We show that an amorphous, buried functionalized molecular squaraine donor layer can undergo an "inverted" quasi-epitaxial growth during postdeposition processing, whereby crystallization is seeded by a subsequently deposited self-assembled nanocrystalline acceptor C_{60} cap layer. We call this apparently unprecedented growth process from a buried interface "inverse quasi-epitaxy" where the crystallites of these "soft" van der Waals bonded materials are only approximately aligned to those of the cap. The resulting crystalline interface hastens charge recombination, thereby reducing the open circuit voltage in an organic photovoltaic cell. The lattice registration also facilitates interdiffusion of the squaraine donor and C_{60} acceptor, which dramatically improves the short circuit current. By controlling the extent to which this crystallization occurs, the voltage losses can be minimized, resulting in power conversion efficiencies of $\eta_P = 5.4 \pm 0.3\%$ for single-junction and $\eta_P = 8.3 \pm 0.4\%$ for tandem small-molecule photovoltaics. This is a general phenomenon with implications for all organic donor–acceptor junctions. That is, epitaxial relationships typically result in a reduction in open circuit voltage that must be avoided in both bilayer and bulk heterojunction organic photovoltaic cells.

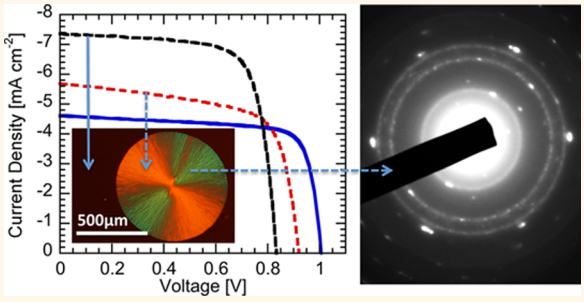

KEYWORDS: epitaxy · organic photovoltaics · solar cell · small molecule · donor–acceptor interface · squaraine · fullerene

Molecular materials form a large class of substances known as "van der Waals solids" due to the eponymously named bond forces that are largely responsible for their intermolecular adhesion. The intrinsic weakness of this bond leads to a low elastic modulus, and when deposited onto a surface, a relatively low adhesive energy between the molecular film and the substrate. The resulting low strain energy between film and substrate allows formation of nano- to macro-crystalline self-organized growth of films that are registered, but not inherently closely lattice matched to the substrate. This is in stark contrast to the growth of more strongly bonded covalent or ionic solids where, in the absence of near-perfect lattice matching, highly defected and disrupted morphologies result. When the lattice constants of the molecular film approximately fit to those of the substrate, oriented crystalline films covering large areas can be achieved.[1−5] The relaxation of the requirement for precise lattice registration between film and substrate results in so-called "quasi-epitaxial" growth.[2] In this work, we demonstrate quasi-epitaxial (q-e) alignment of a buried amorphous organic layer to the lattice of a self-assembled nanocrystalline organic cap layer when entropy is introduced into the system *via* exposure to solvent vapor. We call this process "inverse quasi-epitaxy" since crystallization is initiated at a buried

* Address correspondence to stevefor@umich.edu.

Received for review July 26, 2013 and accepted August 30, 2013.

Published online August 30, 2013
10.1021/nn403897d

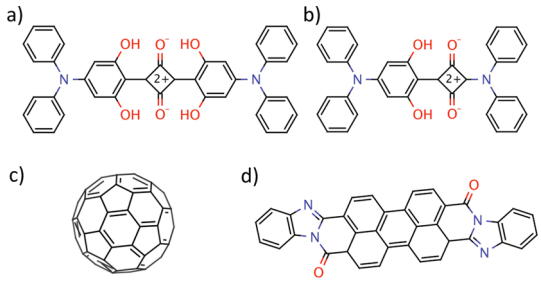

Scheme 1. Molecular structural formulae of the molecules used in this work: (a) DPSQ, (b) DPASQ, (c) C_{60}, and (d) PTCBI.

interface and proceeds throughout the previously deposited layers. This is distinct from the case of conventional epitaxy whereby growth and registration to the substrate lattice occur during deposition at a free surface. Moreover, this "solvent vapor annealing" (SVA) of blends of two archetype functionalized squaraines (see Scheme 1), the asymmetric [2-[4-(*N*,*N*-diphenylamino)-2,6-dihydroxyphenyl]-4-[4-diphenyliminio] squaraine] (DPASQ),[6,7] and the symmetric 2,4-bis[4-(*N*,*N*-diphenylamino)-2,6-dihydroxyphenyl] squaraine (DPSQ), leads to their phase separation, alignment to, and ultimately interdiffusion with a nanocrystalline fullerene (C_{60}) cap. When this donor−acceptor junction is used as the active region in an organic photovoltaic (OPV) cell, a power conversion efficiency of up to $\eta_P = 5.4 \pm 0.3\%$ under 1 sun AM 1.5G illumination (spectrally corrected) is achieved. A similar blended-squaraine/C_{70} junction is incorporated into a tandem OPV cell with $\eta_P = 8.3 \pm 0.4\%$.

It has been shown that OPVs have maximum open-circuit voltages (V_{OC}) equal to the energy offset between the highest occupied molecular orbital (HOMO) of the donor and the lowest unoccupied molecular orbital (LUMO) of the acceptor,[8−10] reduced by the polaron-pair binding energy.[11,12] Typically, however, V_{OC} is reduced from its theoretical maximum value by rapid polaron-pair formation and recombination (at respective rates, k_{rec} and k_{PPr}) that lead to an increase in junction dark current.[11,12] One means to decrease k_{PPr} (and hence minimize the loss in V_{OC}) is to reduce intermolecular orbital overlap at the donor−acceptor (D−A) heterointerface by, for example, employing molecular species that are sterically hindered from close packing.[13,14] Unfortunately, this strategy also inhibits close molecular packing of like molecules in the film bulk, resulting in OPVs with reduced exciton diffusivity and an increased internal electrical resistance. To reduce k_{rec} (*e.g.*, by reducing bimolecular recombination that governs formation of polaron pairs from free carriers[15]), the mobility of the material must be reduced near the interface by, for example, introducing disorder into each layer near the interface, or by mixing of donor and acceptor molecules at the interface. Recently, we demonstrated a technique to *independently* control interface and bulk morphologies by SVA of junctions between DPSQ[6,7] and C_{60} to simultaneously minimize recombination and improve bulk charge transport in bilayer OPVs.[16] We found that when the DPSQ was annealed prior to C_{60} deposition, templating of the C_{60} occurred, and the V_{OC} decreased due to increased k_{rec} and k_{PPr}, as expected for an abrupt interface with close interfacial molecular packing. In contrast, when SVA follows C_{60} deposition, the interface remains disordered, leading to a low k_{rec} and k_{PPr}, and hence, a high V_{OC}, both results being consistent with theoretical predictions of Giebink *et al.*[11,12] Here, we show that when there is sufficiently close lattice matching between layers, SVA of an amorphous as-grown squaraine/fullerene bilayer can lead to inverted q-e growth of the underlying squaraine layer. The lattice registration at the interface is detrimental to device efficiency. Specifically, we find that the bulk morphology and polaron-pair generation and recombination kinetics at the donor−acceptor interface of OPVs, and hence the V_{OC}, is controlled by interface order.

RESULTS

Both DPASQ and DPSQ are chosen for this study since they exhibit strong absorption in the green and near-infrared (NIR) spectral regions, respectively, open circuit voltages approaching $V_{OC} = 1$ V, and efficient energy transport that results in high performance photovoltaic cells.[6,7] When DPSQ films are annealed by exposure to dichloromethane vapor for ~9 min, they crystallize into nanometer-scale domains (see Methods and Materials, and Supporting Information). This roughens the film surface without developing pinholes or voids.[16] In contrast, we find that DPASQ aggressively crystallizes with <4 min exposure to the vapor, resulting in the formation of spherulites (Figure 1a inset). The presence of spherulites indicates a strong driving force for crystallization of the amorphous DPASQ, with highly asymmetric crystal growth rates.[17,18] The spherulite grows from its nucleation site with the fast-crystallization direction oriented radially in the film plane. Growth occurs until the crystallite encounters an energetically relaxed region (*e.g.*, another spherulite), and typically proceeds until the entire film is crystallized (see Figure S1 in Supporting Information).[17,18]

To inhibit spherulite formation and the attendant film roughening, SVA is performed following the deposition of a 40 nm-thick C_{60} acceptor and a 5 nm-thick 3,4,9,10-perylenetetracarboxylic bisbenzimidazole (PTCBI) buffer layer.[19] The reduced density of spherulite nucleation sites results from additional confinement imparted by eliminating the free surface.[16,20] Spherulitic crystallization, however, is not completely suppressed, and the spherulites that nucleate grow to a terminal diameter of 0.5−1.5 mm (Figure 1a, inset). Atomic force microscope images show that the surfaces of the PTCBI above both the spherulite and in the spherulite-free

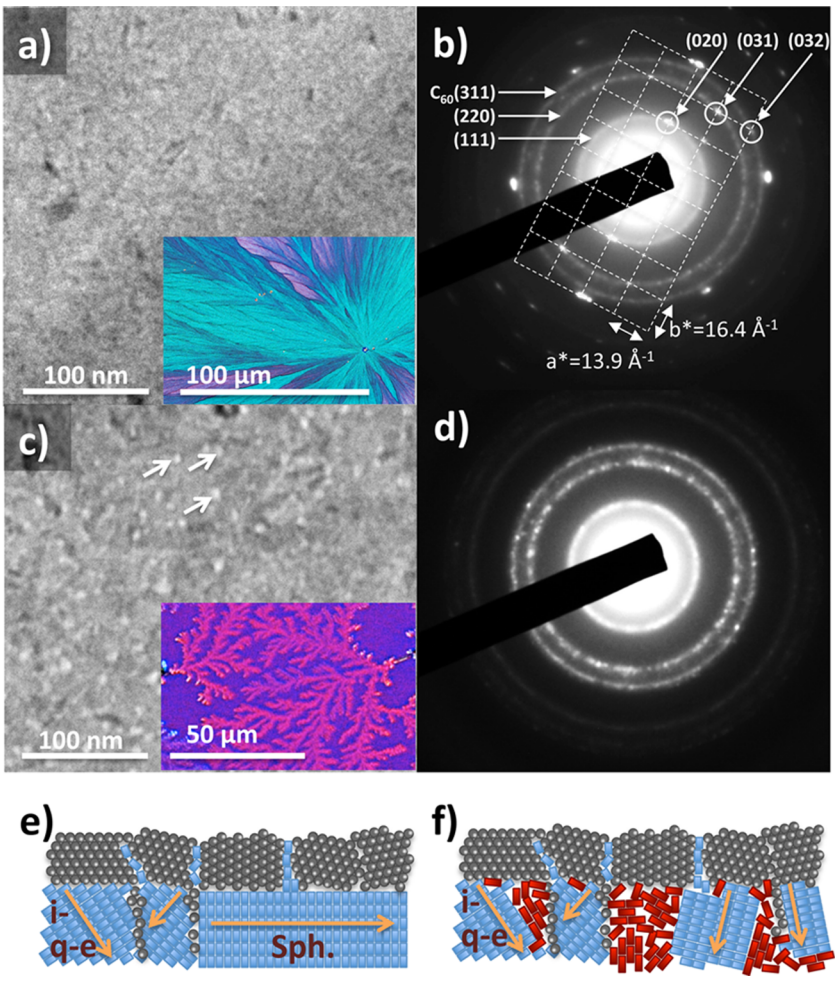

Figure 1. Microstructural analysis of films: (a and c) transmission electron micrographs and (b and d) selected area electron diffraction (SAED) patterns after solvent vapor annealing (SVA) of (a and b) DPASQ/C_{60}/PTCBI spherulite structures and (c and d) blended squaraine/C_{60}/PTCBI layers. (a) Electron micrographs show a relatively unstructured morphology in the spherulite, while (c) mottling in the image of the blend (indicated by arrows) suggests phase separation. Phase-contrast micrographs are inset into (a) showing a spherulite and (b) long-range phase separation, as indicated by dendrite formation of a blended squaraine film. (b) The SAED pattern of DPASQ/C_{60} spherulites indicate single-crystal DPASQ and polycrystalline C_{60} diffraction patterns and the various lattice registrations at the (020), (031), and (032) diffraction conditions (circled); (d) SAED pattern of the blended squaraine film shows decoration of the C_{60} diffraction rings with DPASQ crystallites, but no diffraction from {023} and {040} families of planes. Schematic depictions film structures after SVA of (e) DPASQ/C_{60}, and (f) blended squaraine/C_{60}. The upper layer (circles) depicts the nanocrystalline C_{60} and the lower squaraine layer (rectangles) suggests fast crystallization direction (orange arrows) either in the film plane (thus forming a spherulite, Sph.), or into to the plane of the film (resulting in inverse quasi-epitaxial growth, i-q-e). In the blended squaraine devices (f), the squaraine layer phase separates into a crystalline DPASQ-rich areas (blue rectangles) that interdiffuse into the C_{60} and the DPSQ-rich areas (red rectangles).

regions undergo only minor increases in roughness on SVA (*i.e.*, the root-mean-square roughness increases from $r_{rms} \approx 1.1 \pm 0.1$ nm for the as-cast film to 1.6 ± 0.1 nm for the SVA films).

Transmission electron microscope (TEM) images and selected area electron diffraction (SAED) patterns of a spherulite in a SVA DPASQ/C_{60}/PTCBI layer stack are shown in Figure 1, panels a and b, respectively. The plan-view TEM shows a relatively featureless field, and the SAED pattern shows three uniform rings originating from the (111), (220), and (311) diffraction orders of the as-deposited, polycrystalline C_{60}, along with a rectangular array of spots corresponding to diffraction from a single crystal of DPASQ within a spherulite. The DPASQ has surface unit mesh spacings of $a = 13.9 \pm 0.1$ Å and $b = 16.4 \pm 0.1$ Å offset by 90°. These lattice constants match those measured for a monoclinic single crystal for the *c*-direction (13.99 Å), but indicate an extension of ~2% in the *b*-direction (see Supporting Information). A family of diffraction orders from the single-crystal DPASQ lies on each of the three C_{60} diffraction rings (intersections circled in Figure 1b). Note that the (020) spot has <0.5% mismatch with the C_{60} (111) ring, and near-perfect matching between the (031) and (032) diffraction orders of DPASQ and the (220) and (311) diffraction rings of C_{60}, respectively. Although not visible in Figure 1b, the (100) lattice constant of C_{60} (14.15 Å) has ~1% lattice mismatch

with the (010) lattice constant of DPASQ. This abundance of lattice coincidences results in several possible q-e registrations between the DPASQ and C_{60}.[2,4] This epitaxial relationship is well-defined within the surface plane in one direction (*e.g.*, ⟨020⟩ DPASQ is parallel to ⟨111⟩ C_{60}), but perpendicular relationships are not obvious, suggesting a point-online lattice registration.[21,22] Note, however, that it is not possible to unambiguously identify all preferred alignments between the two crystal lattices since the interface is buried, and hence is inaccessible to surface probes commonly used to identify specific registrations.

The plan-view TEM image in Figure 1c of a similar, but spherulite-free DPASQ:DPSQ blended squaraine layer with a volume ratio of 4:6 that was annealed following the deposition of C_{60} and PTCBI, shows distinct mottling (arrows) that suggests phase separation. Phase separation is also observed after SVA of the bare, blended squaraine films, but on a much larger length scale than in the capped film (see Figure 1c, inset). The SAED pattern in Figure 1d shows only larger Bragg diffraction spots from crystallized DPASQ decorating the C_{60} diffraction rings but not for {023} or {040}, the families of planes with the strongest reflections. From this we infer that the fast crystallite growth must be redirected *into* the film by the C_{60} cap, as opposed to proceeding parallel to the film as in the case of spherulitic growth where there is only coincidental q-e alignment between the blends and the C_{60}. The lack of diffraction from {023} and {040} indicates that the underlying film is not randomly polycrystalline, but only contains grains oriented at specific directions along grains of C_{60}. There is no evidence for inverse q-e of DPSQ, suggesting that only nanocrystalline or amorphous DPSQ phases exist in the blend.

The inverse q-e growth of crystalline domains of DPASQ (molecules indicated by blue rectangles) relative to the C_{60} cap template (gray circles) is illustrated in Figure 1e. Figure 1f depicts phase separation of the squaraine blend followed by inverse q-e growth initiated from the interface with C_{60} that subsequently propagates through the bulk of the DPASQ. Consistent with previous work,[16] the DPSQ (red rectangles) layer has, at best, nanoscale crystallinity; both illustrations suggest interdiffusion of DPASQ and C_{60} (see below).

Current density−voltage (*J*−*V*) characteristics for devices with the structure glass substrate/100 nm indium tin oxide (ITO)/15 nm MoO_3/16 nm DPASQ/40 nm C_{60}/5 nm PTCBI/100 nm Ag are shown for three different film morphologies in Figure 2a and summarized in Table I. As-cast DPASQ/C_{60} devices have V_{OC} = 0.99 ± 0.01 V, short circuit current density of J_{SC} = 4.6 ± 0.2 mA/cm^2, and fill factor of FF = 74 ± 1%, resulting in a power conversion efficiency under simulated 1 sun, AM 1.5G illumination of η_P = 3.4 ± 0.2%. After SVA, two regions are observed: spherulitic and inverse q-e

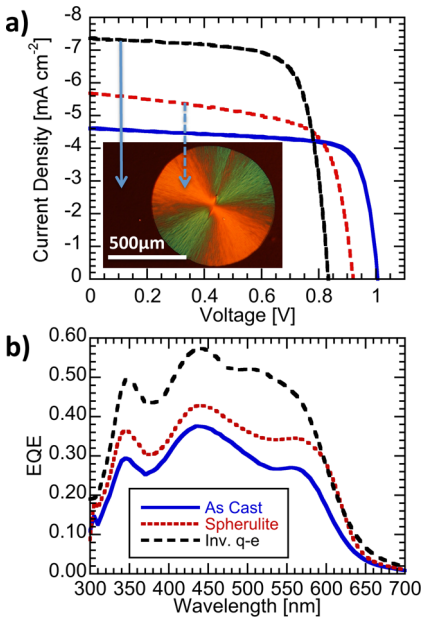

Figure 2. DPASQ/C_{60} photovoltaic cell performance; (a) current−voltage (*J*−*V*) characteristics under 1 sun, simulated AM 1.5G illumination in the 4th quadrant for as-cast (AC, blue line), SVA spherulite (red dotted line), and spherulite-free inverse q-e morphologies (black dashed line) with the inset showing a single DPASQ spherulite and arrows indicating where on a substrate the devices were fabricated; (b) external quantum efficiency (EQE) *vs* wavelength response of the devices in (a).

TABLE I. Efficiency Metrics for DPASQ/C_{60} Devices Fabricated on As-Cast and Solvent Vapor Annealed Films Where Each Device Was Made on a Spherulite or on a Region That Has Undergone Inverse Quasi-Epitaxy (IQE)

device	V_{OC} [V]	J_{SC} [mA/cm^2]	FF [%]	η_P [%]
as-cast	0.99 ± 0.01	4.6 ± 0.2	74 ± 1	3.4 ± 0.2
spherulite	0.92 ± 0.01	5.7 ± 0.3	67 ± 1	3.5 ± 0.2
IQE	0.83 ± 0.01	7.4 ± 0.4	72 ± 1	4.4 ± 0.2

growth areas. The latter regions are uniform in appearance in contrast to those exhibiting spherulitic growth. Devices fabricated on the inverse q-e areas have V_{OC} = 0.83 ± 0.01 V, J_{SC} = 7.4 ± 0.4 mA/cm^2, and FF = 72 ± 1%, with an efficiency of η_P = 4.4 ± 0.2%. The significant drop in V_{OC} that results from the inverse q-e process is indicative of increased orbital overlap between the donor HOMO and acceptor LUMO, and increased Langevin-mediated polaron-pair formation resulting from crystalline, high-mobility material extending to the D−A interface (leading to increased k_{PPr} and k_{rec}, respectively).[11,12] Devices fabricated directly on spherulites are generally electrically shorted; however, in those cases when the devices show diode characteristics, their external quantum efficiency (EQE), J_{SC}, and V_{OC} lie between that of the as-cast and inverse q-e areas, and have slightly lower fill factors with a corresponding efficiency of η_P = 3.5 ± 0.2%. This intermediate V_{OC} results from the increased k_{rec} associated with

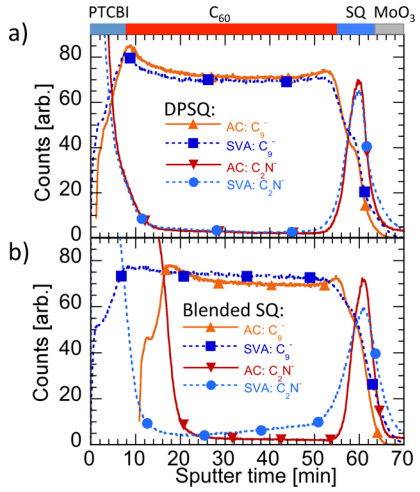

Figure 3. Interdiffusion of squaraine/C_{60} junctions: depth profiles of (a) DPSQ/C_{60}/PTCBI films and (b) blended squaraine/C_{60}/PTCBI films before and after SVA, measured using time-of-flight secondary ion mass spectrometry. The C_2N^- fragment tracks the squaraine and PTCBI concentrations, and C_9^- tracks the C_{60} concentration. The intense C_2N^- signal at the beginning of the scans arises from the PTCBI overlayer.

the improved crystallinity of DPASQ, but poor intermolecular coupling between the DPASQ and C_{60} crystallites caused by the lack of epitaxial alignment. Figure 2b shows the EQE *vs* wavelength (λ) characteristic for the same devices, comparing as-cast, and SVA samples both on spherulites and spherulite-free areas. The EQE increases nearly uniformly across the spectrum in both SVA samples, consistent with the observed changes in J_{SC}.

Time-of-flight secondary ion mass spectrometry (TOF-SIMS) was used to quantify the intermixing[23] of materials in DPSQ/C_{60}/PTCBI stacks and spherulite-free layer stacks of a 4:6 blend of DPASQ:DPSQ/C_{60}/PTCBI (Figure 3). Gaussian-shaped distributions of squaraine (tracked by the C_2N^- signal) are found for both the as-cast (AC) blended squaraine and neat DPSQ layers, whereas the C_{60} distribution (tracked by the C_9^- signal; also produced by the squaraines and PTCBI, albeit at a lower yield) is constant throughout the C_{60} layer. The AC blended DPSQ/C_{60} and DPSQ:DPASQ/C_{60} structures have abrupt interfaces within the experimental resolution limits. Hence, in this case, intermixing is not observed (see below). The slight broadening observed for the DPSQ peak on SVA is predominately a function of the increased roughness at the surface of the stack, but may indicate minor roughening or interdiffusion at the DPSQ/C_{60} interface, which could account for the ~30% increase in photocurrent on SVA (see Supporting Information) In contrast, after a 7 min SVA the blended squaraine/C_{60} structure exhibits a long squaraine tail that penetrates through >30 nm of the C_{60} layer with an average concentration of 4 ± 2 vol %. The C_{60} signal is observed throughout the entire squaraine layer, comprising 18 ± 6 vol % of the mixture, creating two bulk heterojunction-like layers that result in the ~60% increase in EQE compared to the as-cast devices.

By replacing the spherical C_{60} with the rugby-ball-shaped C_{70}, we observe a reduced tendency for spherulite formation on SVA. In these devices, spherulite formation is observed only after >7 min of SVA; the maximum OPV efficiency, however, is achieved after 6 min, approximately double the time needed for analogous C_{60}-based junctions. SAED measurements of a DPASQ/C_{70} structure annealed for 6 min show no evidence of crystallization whatsoever. Similar to the case of DPASQ/C_{60}, J_{SC} for the DPASQ/C_{70} device is increased following SVA; however, the accompanying drop in V_{OC} is only ~0.04 V, or ~25% of that in the C_{60}-based devices (see Supporting Information). This is consistent with the DPSQ/C_{60} system that lacks q-e alignment on SVA following deposition of C_{60}, and hence exhibits no decrease in V_{OC} on SVA. In the case of C_{70}, interfacial molecular orbital overlap is limited by lack of self-organization of the fullerene, and hence, it cannot serve as a template for the underlying squaraine molecules. The markedly reduced interactions of the DPASQ/C_{70} and DPSQ/C_{60} junctions, and the observed differences between the extent of interdiffusion of donors and acceptors for junctions with different crystalline registrations, demonstrate that lattice constant and crystalline mismatch play a significant role in solubility. This is the molecular analogue to the Hume–Rothery model where compounds with well-matched lattice dimensions and crystal structures have an improved solid solubility.[24]

Spherulite formation can also be inhibited by incorporating impurities that form an energetic barrier to crystallization. Here, we have introduced DPSQ as such an impurity that simultaneously extends the absorption of the blend into the NIR. Spherulite formation is frustrated for 10 vol % DPSQ in DPASQ, and completely arrested at 20 vol % DPSQ. Figure 4a is a plot of EQE *vs* wavelength, λ, for OPVs made from various as-cast blends of DPASQ and DPSQ. The EQE contributed from absorption in the C_{60} (*i.e.* $\lambda < 500$ nm) is independent of blend ratio. On addition of 10 vol % DPSQ, response from DPSQ at $\lambda > 650$ nm appears and the EQE arising from absorption in the DPASQ ($\lambda \approx 550$ nm) decreases by ~50% due to trapping of excitons on the lower energy gap DPSQ, thereby reducing exciton diffusivity. Further increases in DPSQ concentration leads to a monotonic increase in NIR response and a decrease in DPASQ response.

Following SVA, all blended devices show significantly increased photosensitivity, with the response at $\lambda \approx 550$ nm roughly proportional to the DPASQ concentration, indicative of the absence of exciton trapping (Figure 4b). All devices with <60 vol % DPSQ show a similar EQE ≈ 58% at $\lambda = 440$ nm resulting from C_{60} absorption, while those with a higher DPSQ

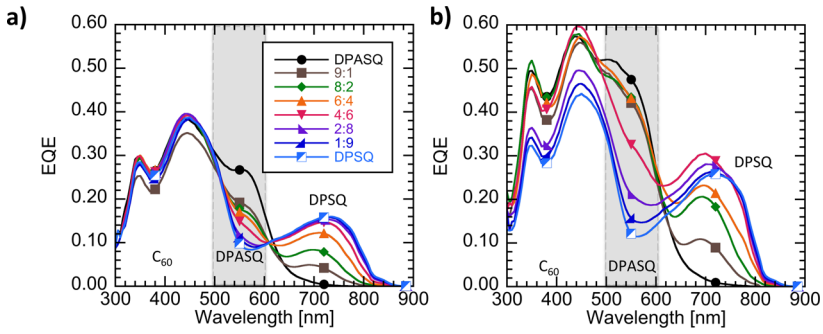

Figure 4. External quantum efficiencies of blended devices: (a) EQE *vs* wavelength for as-cast devices, and (b) SVA devices. The spectral absorption ranges for C_{60}, DPASQ, and DPSQ are labeled for convenience.

concentration have a response approaching that of a DPSQ/C_{60} heterojunction. The EQE arising from DPSQ absorption at $\lambda \approx 750$ nm increases with concentration, reaching a peak EQE = 30% for 60 vol % DPSQ (*i.e.*, 4:6 blend of DPASQ:DPSQ). Further increases in DPSQ concentration lead to a concomitant reduction in response, similar to that of the neat DPSQ/C_{60} junction.[16] The performance characteristics of optimal 4:6 DPASQ:DPSQ/C_{70} OPVs are $V_{OC} = 0.92 \pm 0.01$ V, $J_{SC} = 9.3 \pm 0.5$ mA/cm^2, FF = 63 ± 2%, and $\eta_P = 5.4 \pm 0.3$%. (See Supporting Information for performance data of the blend cells.)

DISCUSSION

The increase in J_{SC} and EQE on SVA of blended DPASQ:DPSQ/C_{60} junctions results from phase separation at a length scale of nanometers, as evidenced by the TEM images (*cf.* Figure 1), and interdiffusion of the DPASQ and C_{60} (Figure 3). This intermixing draws C_{60} into the DPASQ to create fingers of acceptor regions in contact with DPSQ throughout the layer, thereby increasing the internal quantum efficiency (IQE). Since optical wavelengths are much larger than the crystallite dimension or spacing, the incident optical field fully encompasses multiple DPSQ, DPASQ, and C_{60} fingers. The resulting bulk heterojunction prevents the reduction in EQE, as anticipated for a homogeneous donor-layer blend where the absorption of by one species in the blend is reduced in proportion to its volume fraction.

The 4:6 DPASQ:DPSQ/C_{60} device with its broad spectral coverage has been incorporated into a tandem OPV. Figure 5 shows the *J*−*V* and EQE characteristics of a tandem cell designed following previously described methods,[25−27] where the back subcell (that closest to the Ag cathode contact) employs an active layer comprising co-evaporated tetraphenyldibenzoperiflanthene DBP:C_{70} (1:10 vol ratio),[28] and the front subcell (closest to the ITO anode) consists of a SVA blended squaraine (4:6 DPSQ:DPASQ)/C_{70} bulk heterojunction. The optimized tandem structure (see Supporting Information) is: glass substrate/100 nm ITO/20 nm MoO_3/16 nm 4:6 DPASQ:DPSQ/10 nm C_{70}/5 nm PTCBI/0.1 nm Ag/5 nm MoO_3/25 nm DBP:C_{70}/7 nm

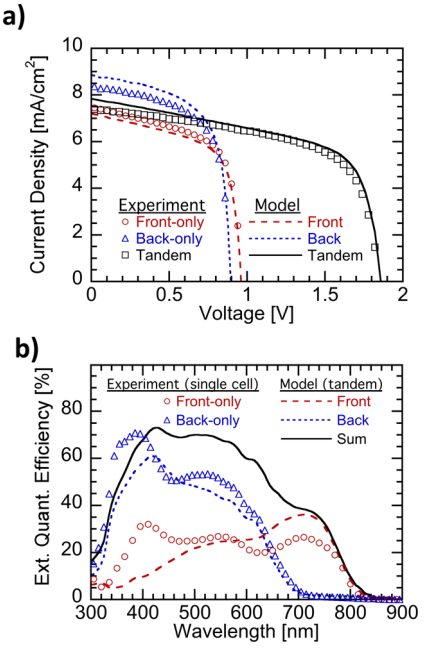

Figure 5. Tandem photovoltaic cell response: (a) experimental *J*−*V* characteristics in the fourth quadrant under 1 sun, simulated AM 1.5G illumination for front-only (circle), back-only (triangle), and tandem (square) organic photovoltaic cells, along with characteristics extrapolated from the model for the front subcell (dashed line) and back subcell (dotted line) for the optical fields in the tandem structure and the predicted tandem (solid line) response; (b) experimental EQE spectra for front-only (circle) and back-only (triangle) organic photovoltaic cells, along with extrapolated spectra for the front subcell (dashed line), back subcell (dotted line), and the sum of the two subcells (solid line).

C_{70}/7 nm bathophenanthroline (BPhen)/100 nm Ag. Figure 5a shows the measured *J*−*V* characteristics for both the discrete cells (circles and triangles), and the tandem device (squares), with $V_{OC} = 1.85 \pm 0.01$ V, FF = 61 ± 1%, $J_{SC} = 7.4 \pm 0.4$ mA/cm^2, and $\eta_P = 8.3 \pm 0.4$%. The lines in Figure 5b show the calculated EQE for each subcell as it behaves in the tandem (red dashed line for the blended squaraine cell, blue dotted line for the DBP:C_{70} cell) and the sum of the EQEs of the subcells (black solid line) showing the overall percent of photons contributing to current in the tandem OPV. The tandem cell

harvests >60% of the photons at $\lambda < 600$ nm, and >40% at $\lambda < 750$ nm.

CONCLUSION

We have shown that self-assembled nanocrystallites of C_{60} template the crystallization of the underlying DPASQ layer. This results in the observation of a possibly general process of a newly observed inverted quasi-epitaxial growth mode, and consequent alignment between the two materials. The q-e alignment results in a registered interface between donor and acceptor molecules, leading to enhanced polaron pair formation and recombination, and hence a reduced V_{OC}. The q-e growth from the interface into the bulk DPASQ is in sharp contrast to the stable, disordered interface that exists for DPSQ/C_{60} and DPASQ/C_{70} junctions, where little to no reduction in V_{OC} is observed on SVA. The DPASQ and C_{60} interdiffuse on SVA to create a bulk heterojunction, whereas interdiffusion of DPSQ and C_{60} is limited. Blending DPSQ into DPASQ/C_{60} devices results in increased J_{SC} and V_{OC} with $\eta_P = 5.4 \pm 0.3\%$ following SVA. By combining blended-squaraine/C_{70} and with DBP/C_{70} co-evaporated cells into a tandem OPV, power conversion efficiencies of $\eta_P = 8.3 \pm 0.4\%$ are obtained. The implications of this study extend well beyond applications to the materials studied here. Quasi-epitaxial alignment between donor and acceptor phases must be avoided in both bilayer and bulk heterojunction OPV cells to maximize the open circuit voltage. Further, we describe successful approaches for eliminating detrimental lattice registration effects.

MATERIALS AND METHODS

Organic photovoltaic (OPV) devices were fabricated on glass substrates precoated with a 100 nm thick layer of indium tin oxide (ITO) previously cleaned by sonicating in detergent and a series of solvents including heated trichloroethylene, acetone, and heated isopropyl alcohol. Substrates were then snow-cleaned to remove particulates[29,30] and subsequently exposed to UV/ozone for 10 min before loading into a vacuum chamber (base pressure $<1 \times 10^{-7}$ Torr) where MoO_3 (15 nm) was thermally deposited at a rate of 0.1 nm/s. Substrates were directly transferred into a high-purity nitrogen-filled glovebox (<10 ppm O_2 and H_2O), where squaraines were cast from solutions of ~1.8 mg/mL of squaraine in chloroform. The squaraines were synthesized, purified, and filtered as described previously.[6,16] A spin-coating ramp rate of 1000 rpm/s with a final speed of 3000 rpm produced ~16 nm-thick films. The 40 nm-thick C_{60} (MER Corp., sublimed grade with one additional purification *via* gradient sublimation purification[2]) and the 8 nm-thick 3,4,9,10- perylenetetracarboxylic bisbenzimidazole (PTCBI, Sensient Technologies Corp. sublimed grade) layer were deposited *via* vacuum thermal evaporation at a rate of 0.1 nm/s. Finally, 100 nm-thick Ag cathodes were deposited through a shadow mask with 1 mm-diameter apertures at a rate of 0.1 nm/s. All organic layer thicknesses were calibrated using variable-angle spectroscopic ellipsometry in their transparent spectral regions.

Solvent vapor annealing was performed after deposition of the PTCBI buffer[19] in 500 mL vials containing an excess of dichloromethane. SVA times of 4 and 9 min were optimal for neat DPASQ and DPSQ layers, respectively, while the optimal for blends was intermediate between that of the neat layers. A 7.5 min SVA was performed on the blended squaraine/C_{70} cell after PTCBI deposition in the tandem device. Details of tandem and DBP:C_{70} device fabrication procedures are described elsewhere.[25,28]

Details of measurements of EQE, electron beam analysis and other materials and device characteristics are found in the Supporting Information

Conflict of Interest: The authors declare the following competing financial interest(s): Two of the authors (MET and SRF) have an equity interest in one of the sponsors of this research (GPEC).

Acknowledgment. The authors gratefully acknowledge S. Wang, and V. V. Diev at the University of Southern California for material synthesis, C. K. Renshaw for technical discussions, and D. Fan for assistance with device fabrication. Funding was provided in part by the Center for Solar and Thermal Energy Conversion at the University of Michigan, an Energy Frontier Research Center funded by the Department of Energy through the Office of Science, Office of Basic Energy Sciences under Award number DE-SC000957 (J.D.Z., experiments and analysis), the SunShot Next Generation Photovoltaics program of Department of Energy (EERE), Award number DE-EE0005310 (B.E.L. tandem design), the collaborative R&D Program with a Technology Advanced Country, [2009-advanced-B-015] by the Ministry of Knowledge and Economy of Korea (X.X., tandem fabrication and testing), the National Science Foundation grant #DMR-0315633 (K.S. and TEM facilities), Global Photonic Energy Corporation (S.R.F, analysis), the Understanding Charge Separation and Transfer at Interfaces in Energy Materials (EFRC:CST), an Energy Frontier Research Center funded by the US Department of Energy, Office of Science, Office of Basic Energy Sciences under Award Number DE-SC000109 (TOF-SIMS, A.D., R.G., K.S. and D.V.B.) and the National Science Foundation grant # DMR-0923096 (TOF-SIMS facility at the Texas Materials Institute). We also acknowledge the support of The Department of Energy, Office of Basic Energy Sciences as part of Energy Frontier Research Center program, the Center for Energy Nanoscience (DE-SC0001013, P.W. and M.E.T., crystallography).

Supporting Information Available: Additional information on methods, experimental data and analysis, details of measurements of EQE, electron beam analysis and other materials and device characteristics. This material is available free of charge *via* the Internet at http://pubs.acs.org.

REFERENCES AND NOTES

1. So, F. F.; Forrest, S. R.; Shi, Y. Q.; Steier, W. H. Quasi-Epitaxial Growth of Organic Multiple Quantum Well Structures by Organic Molecular-Beam Deposition. *Appl. Phys. Lett.* **1990**, *56*, 674–676.
2. Forrest, S. R. Ultrathin Organic Films Grown by Organic Molecular Beam Deposition and Related Techniques. *Chem. Rev.* **1997**, *97*, 1793–1896.
3. Schmitz-Hubsch, T.; Sellam, F.; Staub, R.; Torker, M.; Fritz, T.; Kubel, C.; Mullen, K.; Leo, K. Direct Observation of Organic-Organic Heteroepitaxy: Perylene-Tetracarboxylic-Dianhydride on Hexa-Peri-Benzocoronene on Highly Ordered Pyrolytic Graphite. *Surf. Sci.* **2000**, *445*, 358–367.
4. Mannsfeld, S. C. B.; Leo, K.; Fritz, T. Line-on-Line Coincidence: A New Type of Epitaxy Found in Organic-Organic Heterolayers. *Phys. Rev. Lett.* **2005**, *94*, 056104.
5. Lunt, R. R.; Sun, K.; Kroger, M.; Benziger, J. B.; Forrest, S. R. Ordered Organic-Organic Multilayer Growth. *Phys. Rev. B* **2011**, *83*, 064114.
6. Wang, S.; Hall, L.; Diev, V. V.; Haiges, R.; Wei, G.; Xiao, X.; Djurovich, P. I.; Forrest, S. R.; Thompson, M. E. N,N-Diaryl-anilinosquaraines and Their Application to Organic Photovoltaics. *Chem. Mater.* **2011**, *23*, 4789–4798.

7. Wei, G. D.; Xiao, X.; Wang, S. Y.; Sun, K.; Bergemann, K. J.; Thompson, M. E.; Forrest, S. R. Functionalized Squaraine Donors for Nanocrystalline Organic Photovoltaics. *ACS Nano* **2012**, *6*, 972–978.
8. Rand, B. P.; Burk, D. P.; Forrest, S. R. Offset Energies at Organic Semiconductor Heterojunctions and Their Influence on the Open-Circuit Voltage of Thin-Film Solar Cells. *Phys. Rev. B* **2007**, *75*, 115327.
9. Brabec, C. J.; Cravino, A.; Meissner, D.; Sariciftci, N. S.; Fromherz, T.; Rispens, M. T.; Sanchez, L.; Hummelen, J. C. Origin of the Open Circuit Voltage of Plastic Solar Cells. *Adv. Funct. Mater.* **2001**, *11*, 374–380.
10. Scharber, M. C.; Mühlbacher, D.; Koppe, M.; Denk, P.; Waldauf, C.; Heeger, A. J.; Brabec, C. J. Design Rules for Donors in Bulk-Heterojunction Solar Cells—Towards 10% Energy-Conversion Efficiency. *Adv. Mater.* **2006**, *18*, 789–794.
11. Giebink, N. C.; Wiederrecht, G. P.; Wasielewski, M. R.; Forrest, S. R. Ideal Diode Equation for Organic Heterojunctions. I. Derivation and Application. *Phys. Rev. B* **2010**, *82*, 155305.
12. Giebink, N. C.; Lassiter, B. E.; Wiederrecht, G. P.; Wasielewski, M. R.; Forrest, S. R. Ideal Diode Equation for Organic Heterojunctions. II. The Role of Polaron Pair Recombination. *Phys. Rev. B* **2010**, *82*, 155306.
13. Perez, M. D.; Borek, C.; Forrest, S. R.; Thompson, M. E. Molecular and Morphological Influences on the Open Circuit Voltages of Organic Photovoltaic Devices. *J. Am. Chem. Soc.* **2009**, *131*, 9281–9286.
14. Schlenker, C. W.; Barlier, V. S.; Chin, S. W.; Whited, M. T.; McAnally, R. E.; Forrest, S. R.; Thompson, M. E. Cascade Organic Solar Cells. *Chem. Mater.* **2011**, *23*, 4132–4140.
15. Groves, C.; Greenham, N. C. Bimolecular Recombination in Polymer Electronic Devices. *Phys. Rev. B* **2008**, *78*, 155205.
16. Zimmerman, J. D.; Xiao, X.; Renshaw, C. K.; Wang, S. Y.; Diev, V. V.; Thompson, M. E.; Forrest, S. R. Independent Control of Bulk and Interfacial Morphologies of Small Molecular Weight Organic Heterojunction Solar Cells. *Nano Lett.* **2012**, *12*, 4366–4371.
17. Keith, H. D.; Padden, F. J. A Phenomenological Theory of Spherulitic Crystallization. *J. Appl. Phys.* **1963**, *34*, 2409–2421.
18. Granasy, L.; Pusztai, T.; Tegze, G.; Warren, J. A.; Douglas, J. F. Growth and Form of Spherulites. *Phys. Rev. E* **2005**, *72*, 011605.
19. Lassiter, B. E.; Wei, G.; Wang, S.; Zimmerman, J. D.; Diev, V. V.; Thompson, M. E.; Forrest, S. R. Organic Photovoltaics Incorporating Electron Conducting Exciton Blocking Layers. *Appl. Phys. Lett.* **2011**, *98*, 243307.
20. Peumans, P.; Uchida, S.; Forrest, S. R. Efficient Bulk Heterojunction Photovoltaic Cells Using Small-Molecular-Weight Organic Thin Films. *Nature* **2003**, *425*, 158–162.
21. Hoshino, A.; Isoda, S.; Kurata, H.; Kobayashi, T. Scanning Tunneling Microscope Contrast of Perylene-3,4,9,10-Tetracarboxylic-Dianhydride on Graphite and Its Application to the Study of Epitaxy. *J. Appl. Phys.* **1994**, *76*, 4113–4120.
22. Mannsfeld, S. C. B.; Fritz, T., Analysis of the Substrate Influence on the Ordering of Epitaxial Molecular Layers: The Special Case of Point-on-Line Coincidence. *Phys. Rev. B* **2004**, *69*.
23. Treat, N. D.; Brady, M. A.; Smith, G.; Toney, M. F.; Kramer, E. J.; Hawker, C. J.; Chabinyc, M. L. Correction: Interdiffusion of Pcbm and P3ht Reveals Miscibility in a Photovoltaically Active Blend. *Adv. Energy Mater.* **2011**, *1*, 145.
24. Hume-Rothery, W.; Powell, H. M. *Z. Kristallogr.* **1935**, *91*, 23–46.
25. Lassiter, B. E.; Zimmerman, J. D.; Panda, A.; Xiao, X.; Forrest, S. R. Tandem Organic Photovoltaics Using Both Solution and Vacuum Deposited Small Molecules. *Appl. Phys. Lett.* **2012**, *101*, 063303.
26. Renshaw, C. K.; Zimmerman, J. D.; Lassiter, B. E.; Forrest, S. R. Photoconductivity in Donor-Acceptor Heterojunction Organic Photovoltaics. *Phys. Rev. B* **2012**, *86*, 085324.
27. Jeong, W. I.; Lee, Y. E.; Shim, H. S.; Kim, T. M.; Kim, S. Y.; Kim, J. J. Photoconductivity of C_{60} as an Origin of Bias-Dependent Photocurrent in Organic Photovoltaics. *Adv. Funct. Mater.* **2012**, *22*, 3089–3094.
28. Xiao, X.; Zimmerman, J. D.; Lassiter, B. E.; Bergemann, K. J.; Forrest, S. R. A Hybrid Planar-Mixed Tetraphenyldibenzoperiflanthene/C_{70} Photovoltaic Cell. *Appl. Phys. Lett.* **2013**, *102*, 073302.
29. Wang, N. N.; Zimmerman, J. D.; Tong, X. R.; Xiao, X.; Yu, J. S.; Forrest, S. R. Snow Cleaning of Substrates Increases Yield of Large-Area Organic Photovoltaics. *Appl. Phys. Lett.* **2012**, *101*, 133901.
30. Sherman, R.; Grob, J.; Whitlock, W. Dry Surface Cleaning Using Co_2 Snow. *J. Vac. Sci. Technol., B* **1991**, *9*, 1970–1977.